Schweizerischer Erdbebendienst
Service Sismologique Suisse
Servizio Sismico Svizzero
Swiss Seismological Service

ETH zürich

SITE CHARACTERIZATION REPORT

SKLW: Kloten (ZH) - Waffenplatz

Manuel Hobiger, Paolo Bergamo, Stefano Maranò, Clotaire Michel, Jan Burjánek, Marco Pilz, Donat Fäh

Last Modification: 16th September, 2016

Schweizerischer Erdbebendienst (SED)
Service Sismologique Suisse
Servizio Sismico Svizzero
Servizi da Terratrembels Svizzer

ETH Zürich
Sonneggstrasse 5
8092 Zürich
Schweiz
manuel.hobiger@sed.ethz.ch

Contents

1 Summary

The new strong-motion station SKLW was built on the Waffenplatz in Kloten, adjacent to the airport of Zurich. It replaces station SZUF of the old strong motion network, which was located about 1 km distant in the center of the airport areal. In order to characterize the site of station SKLW, we performed passive seismic array measurements with two configurations and additional active seismic measurements by sledgehammering. The measurements showed that the fundamental frequency of the ground structure is 2.5 Hz. No 2-dimensional site effects were detected. The seismic refraction measurement fixes the dephts of two superficial layers shallower than 3 m. Using different techniques (3C-HRFK, WaveDec, SPAC), consistent dispersion curves are measured for Love and Rayleigh waves. For Rayleigh waves, also a part of the dispersion curve for the first harmonic mode is measured. The Rayleigh wave ellipticity curve shows a singular peak around 2.5 Hz and a singular trough around 6.5 Hz. A joint inversion of the different measured data results in similar models for the superficial 50 m of structure with an average V_{S30} of 402 m/s. The bedrock starts at around 60 to 100 m depth.

2 Introduction

In the framework of the second phase of the Swiss Strong Motion Network (SSMNet) renewal project, a replacement for station SZUF (running from 09/04/1998 to 06/05/2009) at the airport of Zurich was planned. SZUF was located inside a transformer house and an installation of a new station outside of this transformer house was not possible due to the uncertainty if this location would be in a low-level moor or not. Waiting for an airport project to remeasure all moor areas would have meant a delay of at least two years. Therefore it was decided to find a new location in the vicinity of the airport. Finally, it was decided to construct the new station SKLW next to a chalet on the Waffenplatz of Kloten, which is just adjacent to the airport. The new station is located around 1 km in eastsoutheastern direction from the old station. It went operational on 29 May 2015. At the new location, the station is even closer to the airport's main buildings than the old one.

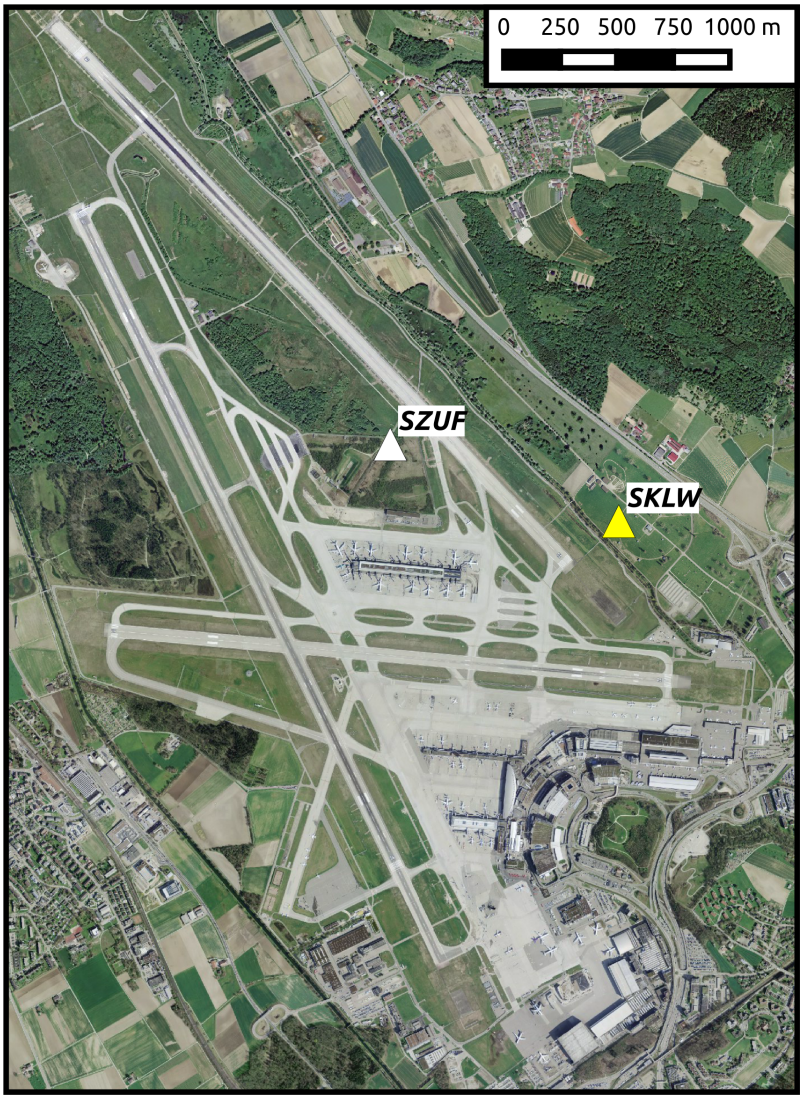

Figure 1: Map showing the airport of Zurich with the locations of the old station SZUF and the new station SKLW.

3 Site characterization

3.1 Measurements and data set

The local underground structure at station SKLW was investigated by different passive and active methods on 25 September 2015. Two passive arrays were set up, the first one consisted of 16 seismic sensors, the second one of 12 sensors. The sensor locations had been previously optimized with the algorithm of Maranò et al. (2014). The sizes of the two arrays were selected in such a way that the array responses do not overlap much so that the widest possible frequency range can be analyzed.
In addition, we deployed a line of geophones inside the first array and performed active measurements by sledgehammering. During these measurements at the fourth shot point, the trigger got broken and we could not continue these measurements. Furthermore, we hammered at several other locations inside the first array and tried to analyze the data recordings of the passive array using the algorithm presented in Maranò et al. (2016), but the method is still in a test stage and the results of this processing are not included in this report. The locations of all seismic stations of the passive and active measurements as well as the hammer shot points are shown in Figs 2 and 3. The respective parameters are given in Tables 1, 2 and 3. The station names in the arrays are "SKLW" followed by a two-digit number, where stations in the first array have numbers between 1 and 31 and in the second array between 51 and 62. Station SKLW02 was the closest one to station SKLW and serves as a reference measurement for the single-station methods. The hammer shot locations are called HAMMER1 to HAMMER11.
The station locations have been measured by a differential GPS system (Leica Viva GS10) which was set up to measure with a precision better than 5 cm. Finally, the largest error of a station location was 2.6 cm.

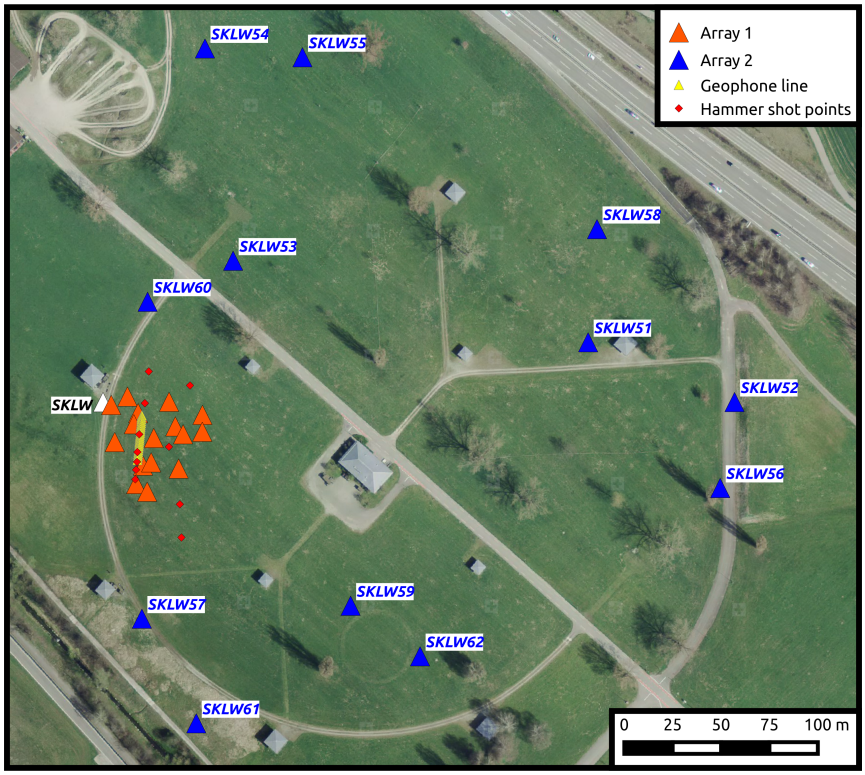

Figure 2: Layout of the measurements around station SKLW.

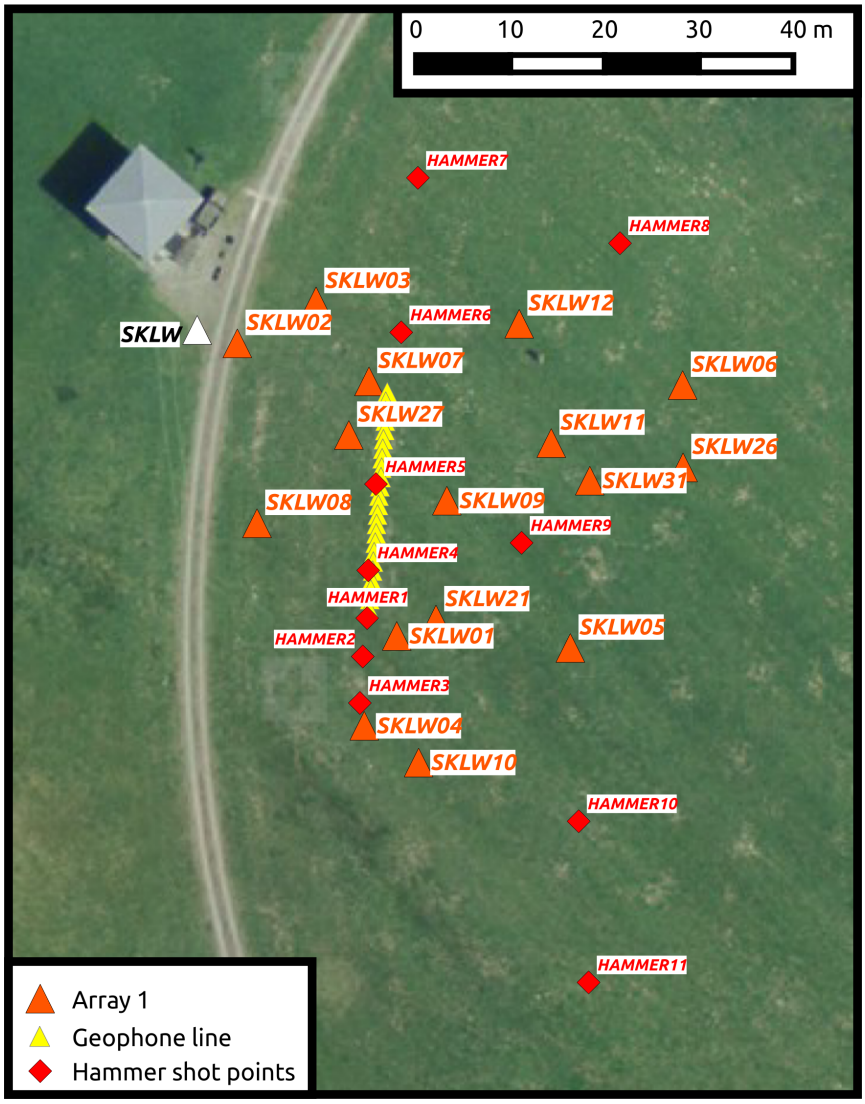

Figure 3: Layout of the measurements around station SBAS with a zoom on the first array. The stations of the second array are not shown.

Table 1: List of the passive seismic measurements.

Array name	Number of sensors	Minimum interstation distance [m]	Maximum interstation distance [m]	Recording time [s]
1	16	4.5	50.1	8100
2	12	44.3	349.5	7260

Table 2: List of the active seismic measurements recorded on the geophone line.

Shot point	Number of shots	Distance from geophone line [m]	Geophone spacing [m]
HAMMER1	11	1.0	1.0
HAMMER2	10	5.0	1.0
HAMMER3	10	10.0	1.0
HAMMER4	7	in the line	1.0

Table 3: List of the active seismic measurements recorded on the passive array. The mininum and maximum distances between the shot point and any array station are also indicated.

Shot point	Number of shots	Minimum distance from sensor [m]	Maximum distance from sensor [m]
HAMMER1	11	3.7	41.6
HAMMER2	10	4.2	44.5
HAMMER3	10	2.5	48.0
HAMMER4	12	7.6	38.7
HAMMER5	10	5.9	34.2
HAMMER6	10	6.2	45.6
HAMMER7	10	17.0	61.9
HAMMER8	10	13.7	59.0
HAMMER9	10	9.1	36.8
HAMMER10	10	18.1	62.2
HAMMER11	11	29.5	77.7

3.2 Single-station measurement results

3.2.1 H/V curves

Figure 4 shows the H/V curves determined with the time-frequency analysis method (Fäh et al., 2009) for all stations of both arrays. For the first array, all stations except two are in very good agreement and there is a first peak at around 0.75 Hz and a second peak around 2.45 Hz. The station with the large peak is SKLW21, which is located in the centre of the array. It is unclear why this station shows a very similar curve to all other stations above 2.5 Hz, but a completely different amplitude below.
For the second array, the curves are more scattered. The first peak is still around 0.75 Hz for all stations, but the second peak ranges from 2.5 to over 10 Hz. This indicates lateral heterogeneities in the superficial structure, but a rather homogeneous structure at depth.

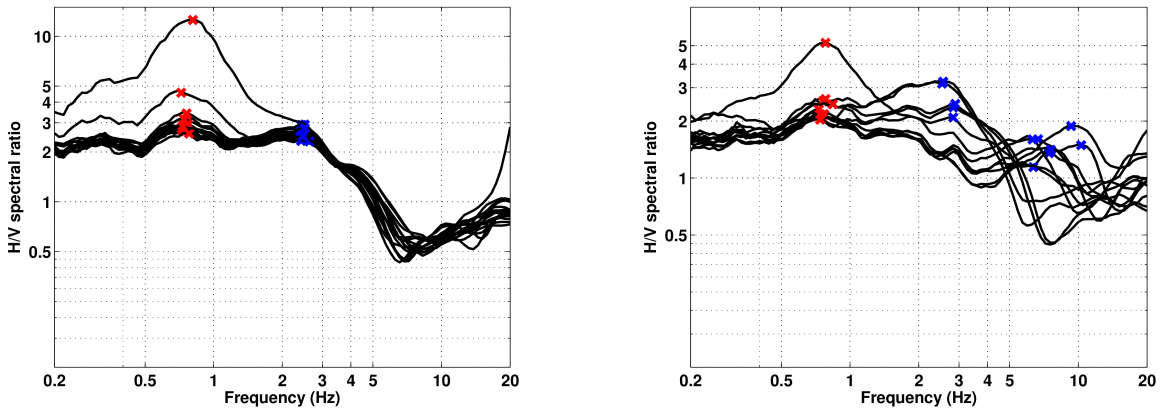

Figure 4: Overview of the H/V measurements for the different stations of first array measurement (left) and the second array measurement (right).

3.2.2 RayDec ellipticity curves

The RayDec technique (Hobiger et al., 2009) is meant to eliminate the contributions of other wave types than Rayleigh waves and give a better estimate of the ellipticity than the classical H/V technique. The RayDec ellipticity curves for all stations of the array measurements are shown in Fig. 5.
Here again, the curves for the different stations in the small array are in very good agreement with each other. Station SKLW21, which is located in the center of the array, is an outlier and shows a very strange behavior that was already visible in the H/V curves. The ellipticity peak at 2.45 Hz might be a singular peak together with a singular trough at 6.7 Hz, but this cannot be finally determined from the RayDec curves. For the large array, the curves for the different stations are quite different from each other.

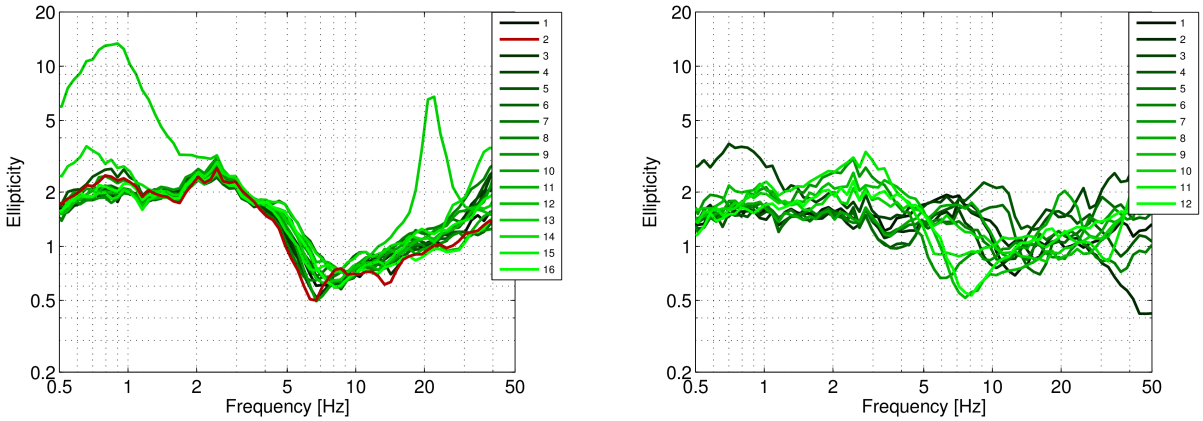

Figure 5: RayDec ellipticities for array 1 (left) and array 2 (right).

3.2.3 Polarization measurements

The polarization parameters of the seismic noise recordings of all stations of the two arrays are similar and do not show significantly polarized particle motions. As an example, the polarization analysis results for station SKLW02 are shown in Fig. 6. The analysis was performed according to Burjánek et al. (2010) and Burjánek et al. (2012). The particle motion has no significant polarization and there are no preferred strike directions, i.e. there is no 2- or 3-dimensional wave propagation effect in the valley. As the sedimentary basin is about 2 to 3 km wide and around 60 m deep (as determined by the final inversion), the basin is expected to behave like a 1-dimensional structure.

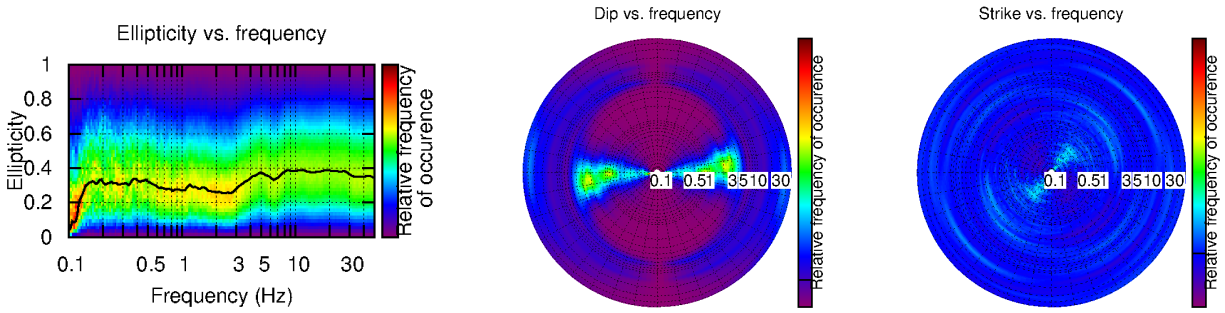

Figure 6: Polarization analysis of station SKLW02.

3.3 Passive array processing results

3.3.1 3-component high-resolution FK

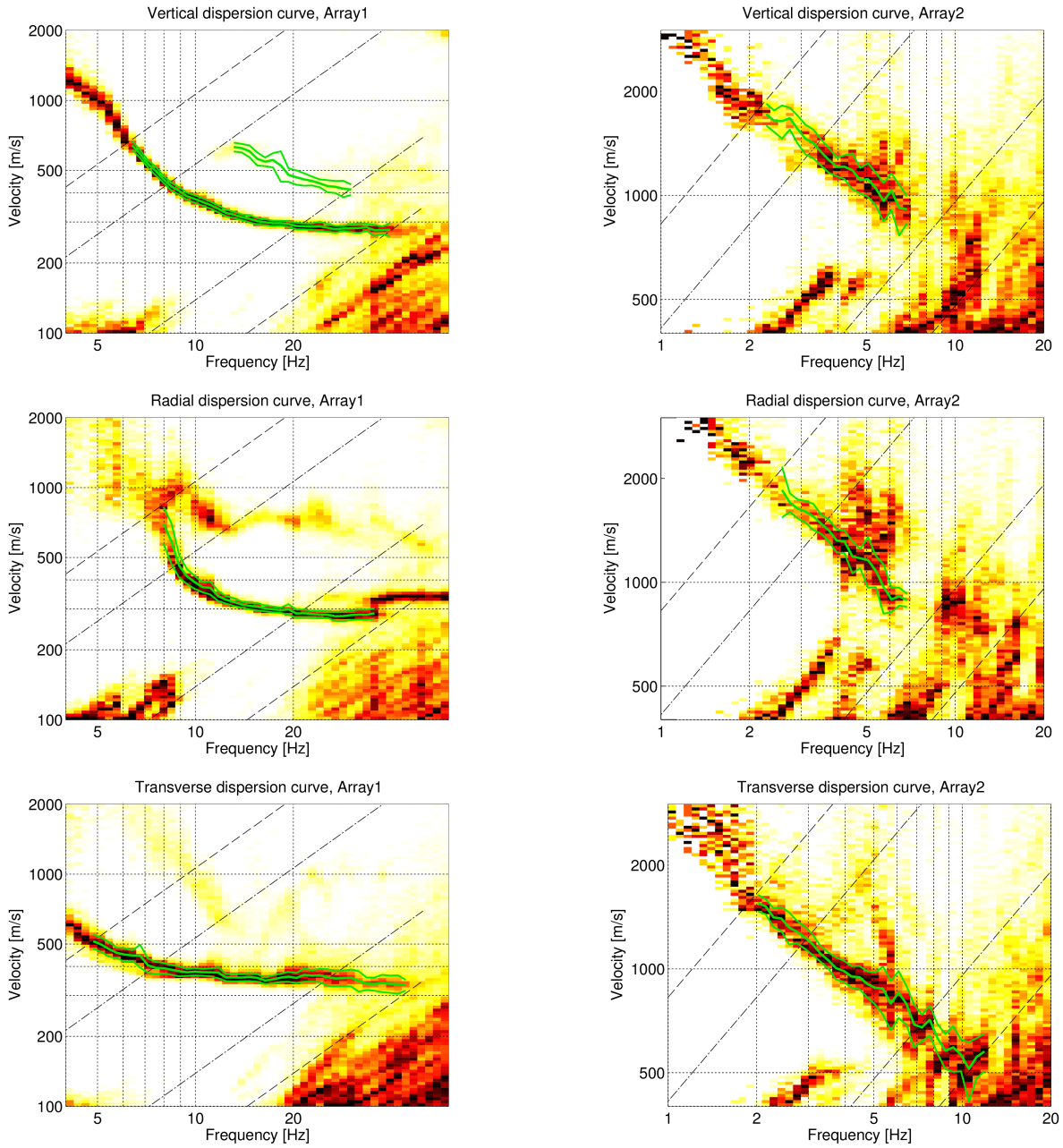

Figure 7: Dispersion curves obtained with the 3-component HRFK algorithm (Poggi and Fäh, 2010). In the left column, the results for array 1 are shown, in the right column for array 2. The lines from top to bottom show the results for the vertical, radial and transverse components, respectively. The dashed and dotted black lines are the array resolution limits. The solid green lines are picked from the data, where the central line indicates the best values and the two outer lines the standard deviation.

The dispersion curves obtained by the 3-component high-resolution FK analysis (Poggi and Fäh, 2010) for both arrays are shown in Fig. 7. On the vertical component, a continuous dispersion curve is clearly visible in array 1 over the whole resolvable frequency

range. It is similarly visible on the radial component as well. A higher mode is visible on the vertical, but not on the radial component. In the larger array, the results are less clear, but dispersion curves can also be retrieved on the vertical and the radial components up to 7 Hz. Here, the upper resolution limit is not reached.
The fundamental Love wave dispersion curve is well retrieved on both arrays in the whole resolvable frequency range. The ellipticity curves determined with the 3-component HRFK analysis are shown in Fig. 8.

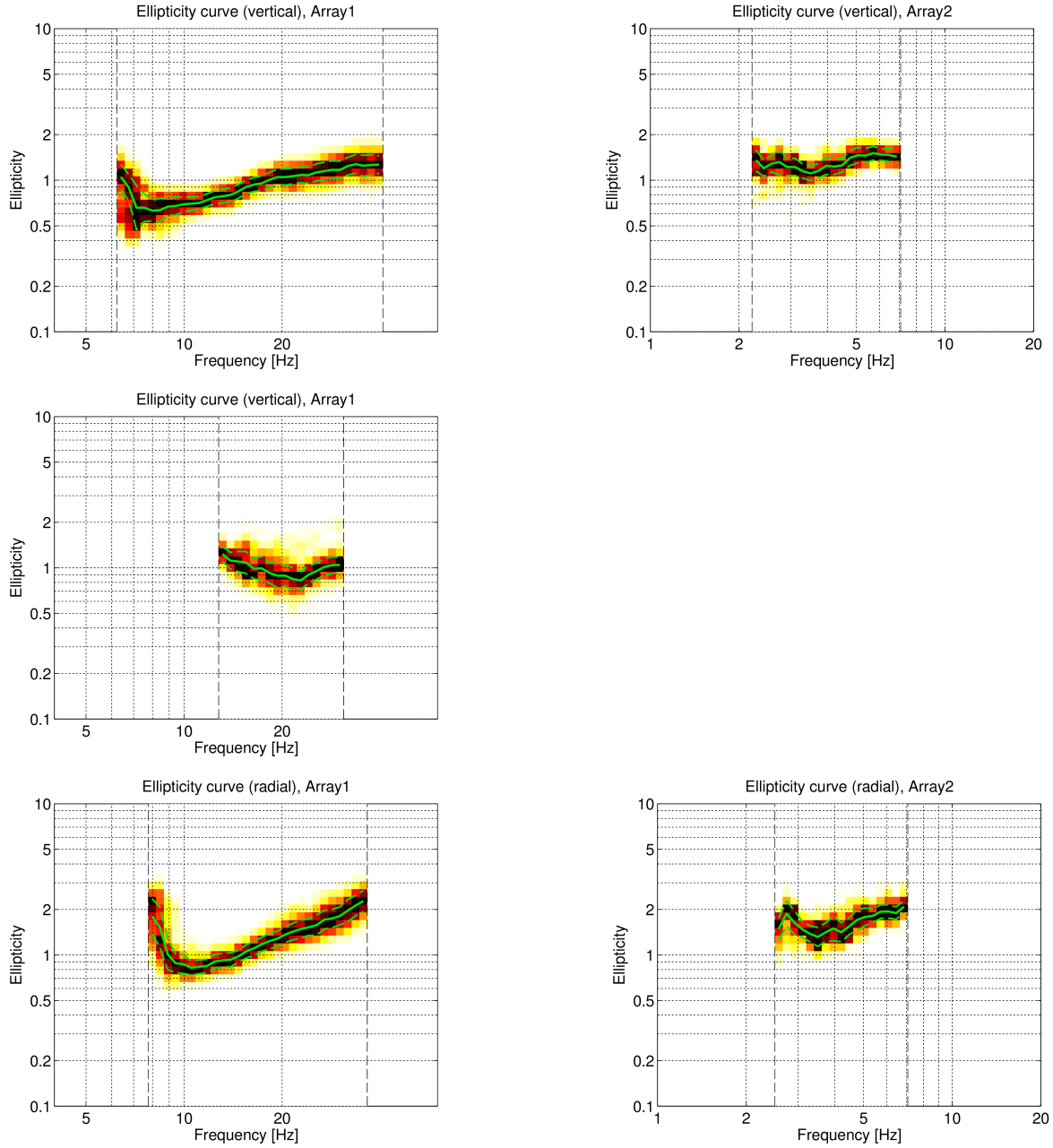

Figure 8: Ellipticity curves obtained with the 3-component HRFK algorithm (Poggi and Fäh, 2010) for array 1 (left) and array 2 (right). The frequency ranges of the different curves correspond to the ranges where the dispersion curves had been picked. Top: Results for the vertical component (first mode). Center: Results for the vertical component (second mode). Bottom: Results for the radial component.

3.3.2 WaveDec

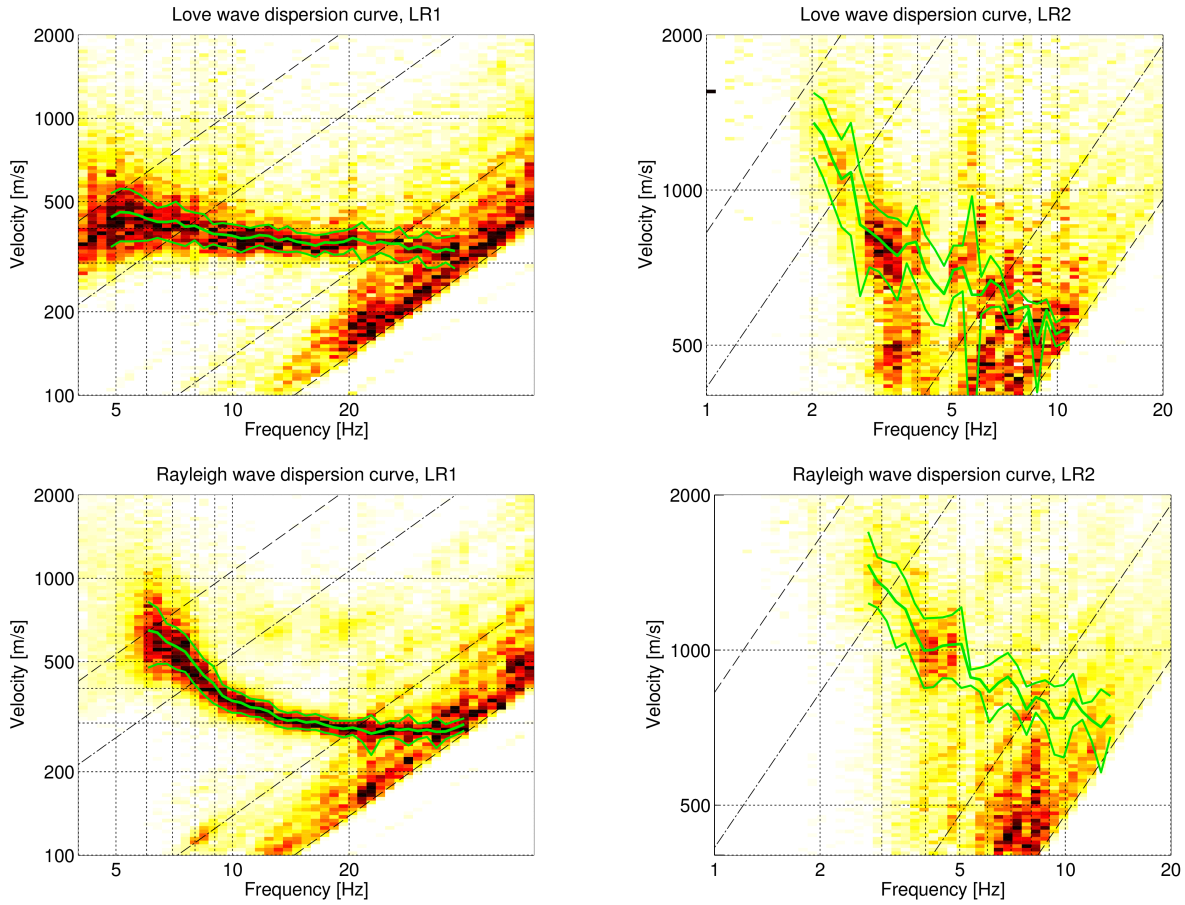

Figure 9: Dispersion curves obtained with the WaveDec technique (Maranò et al., 2012). The Love wave dispersion curves are shown in the top line, the Rayleigh wave dispersion curves in the bottom line. The left plots correspond to array 1, the right ones to array 2. The dashed lines indicate the theoretical array resolution limits.

The results of the WaveDec (Maranò et al., 2012) processing are shown in Figs 9 and 10. This technique estimates the properties of single or multiple waves simultaneously with a maximum likelihood approach. We applied it modeling up to three waves, Love and/or Rayleigh waves, at the same time.
The Love wave dispersion curve is well retrieved in array 1 over the whole accessible frequency range, but less clearly in array two. The results for Rayleigh waves are similar, the retrieval is much better in array 1. For both Love and Rayleigh waves, we cannot determine higher modes.
The ellipticity curves in Fig. 10 are plotted in two ways. In the top line, the ellipticity angle is shown. In the bottom line, the ellipticity is shown. The WaveDec code actually estimates the ellipticity angle. Ellipticity is the absolute value of the tangent of this angle. A negative ellipticity angle stands for retrograde particle motion, a positive ellipticity angle for prograde particle motion.
For array 1, the particle motion is prograde below 7 Hz, but unfortunately the lower array resolution limit prevents us from going much lower than this frequency, so that we cannot see what happens below that frequency. Above 7 Hz and up to about 35 Hz, the particle motion is retrograde. As we assume that we see the fundamental Rayleigh wave

mode here, this would indicate a singular trough around 7 Hz. As the particle motion of the fundamental mode is retrograde at low frequencies, there must also be a singular peak below 7 Hz which we cannot determine with WaveDec.
With array 2, it would be in principle possible to access lower frequencies, but the results are strange. Between 2.6 and 6.2 Hz, the ellipticity angle is retrieved around $\pm 90^\circ$, i.e. the vertical component vanishes and the ellipticity has a singularity. In any case, this is a very unusual behaviour and questions the quality of these data. In any case, the H/V curves of the second array showed differences for the different stations which indicate lateral variations. The WaveDec approach does not work well in such a setting.

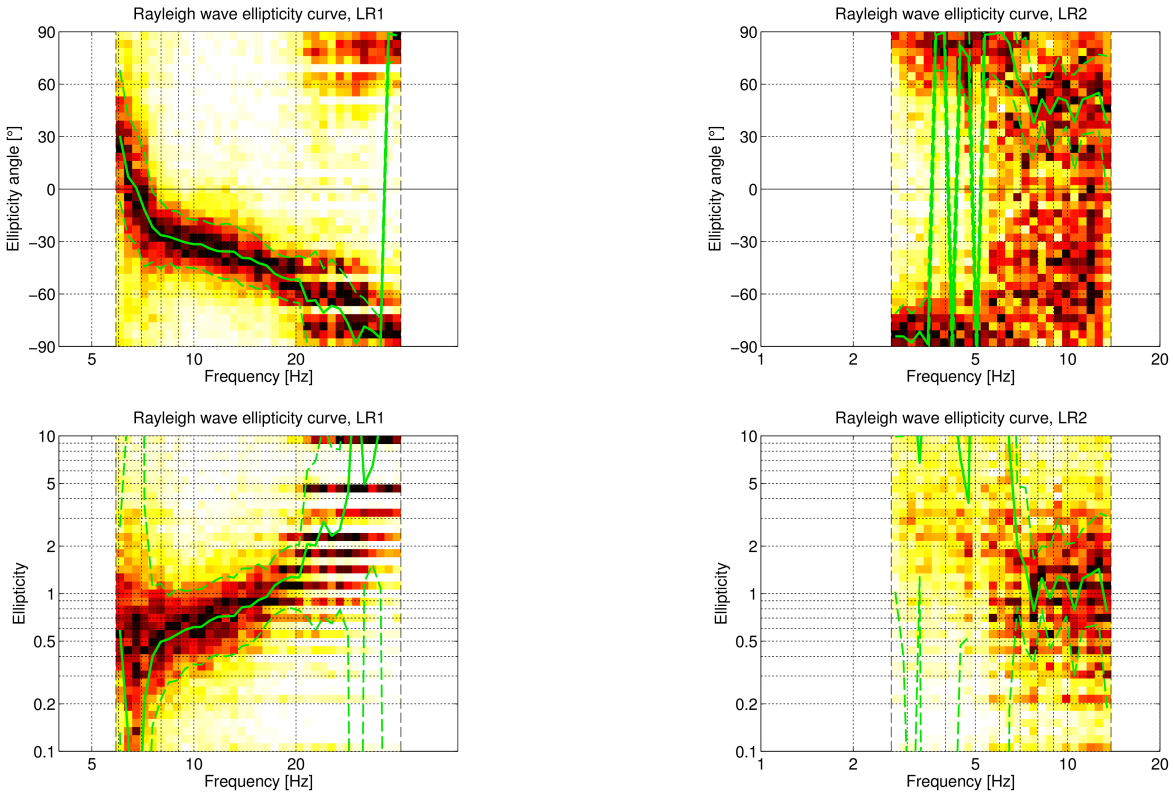

Figure 10: Rayleigh wave ellipticity curves obtained with the WaveDec technique (Maranò et al., 2012). The left column shows the results for array 1, the right column for array 2. The top line represents the ellipticity angles, the bottom line the tangent of this angle, i.e. the ellipticity.

3.3.3 SPAC

For both arrays, we also calculated the SPAC (Aki, 1957) curves of the vertical components, using the M-SPAC (Bettig et al., 2001) technique implemented in geopsy. In order to do so, rings with different radius ranges have been defined. For all station pairs with distance inside this radius range, the cross-correlation is calculated in different frequency ranges. These cross-correlation curves are averaged for all station pairs of the respective ring and give the SPAC curve. The rings are defined in such a way that at least three station pairs contribute and that their connecting vectors have a good directional coverage.
The resulting dispersion curves for SPAC are shown in Fig. 11. The SPAC curves for all defined rings are shown in Figs 12 and 13, respectively, where the black points indicate the data values which contributed to the final dispersion curve estimations by the function `spac2disp` of the geopsy package. For array 1, SPAC yields very nice Bessel functions and the dispersion curve is retrieved between 2.2 and 15.2 Hz. For array 2, the SPAC curves are also of good quality and a dispersion curve can be retrieved between 1.3 and 9.3 Hz.

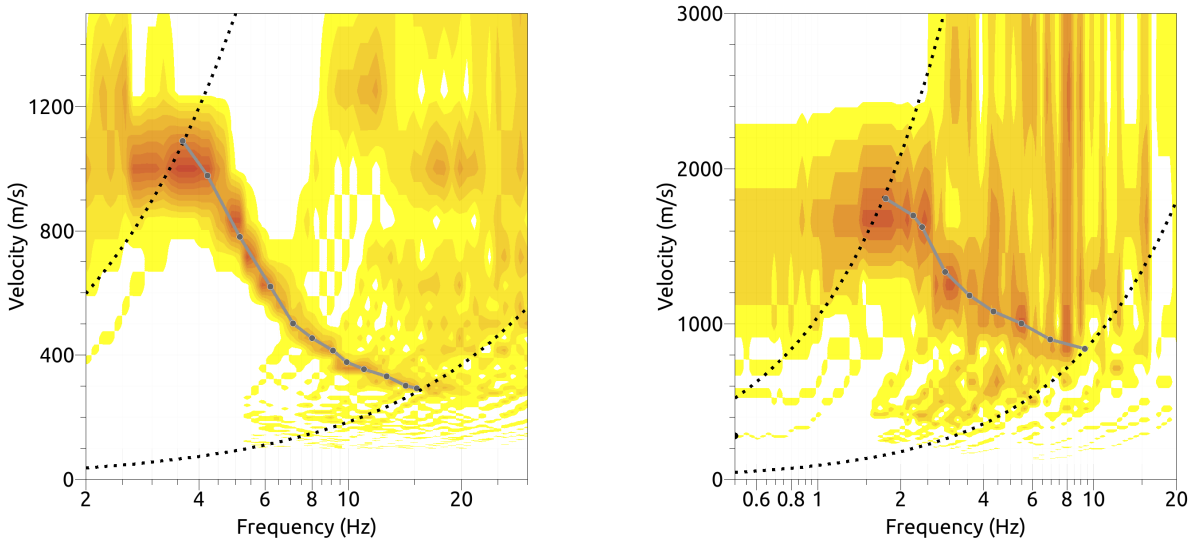

Figure 11: Resulting Rayleigh wave velocities for array 1 (left) and array2 (right). The gray line corresponds to the picked dispersion curve. The black dotted curves are resolution limits, which are different from the FK analysis resolution limits.

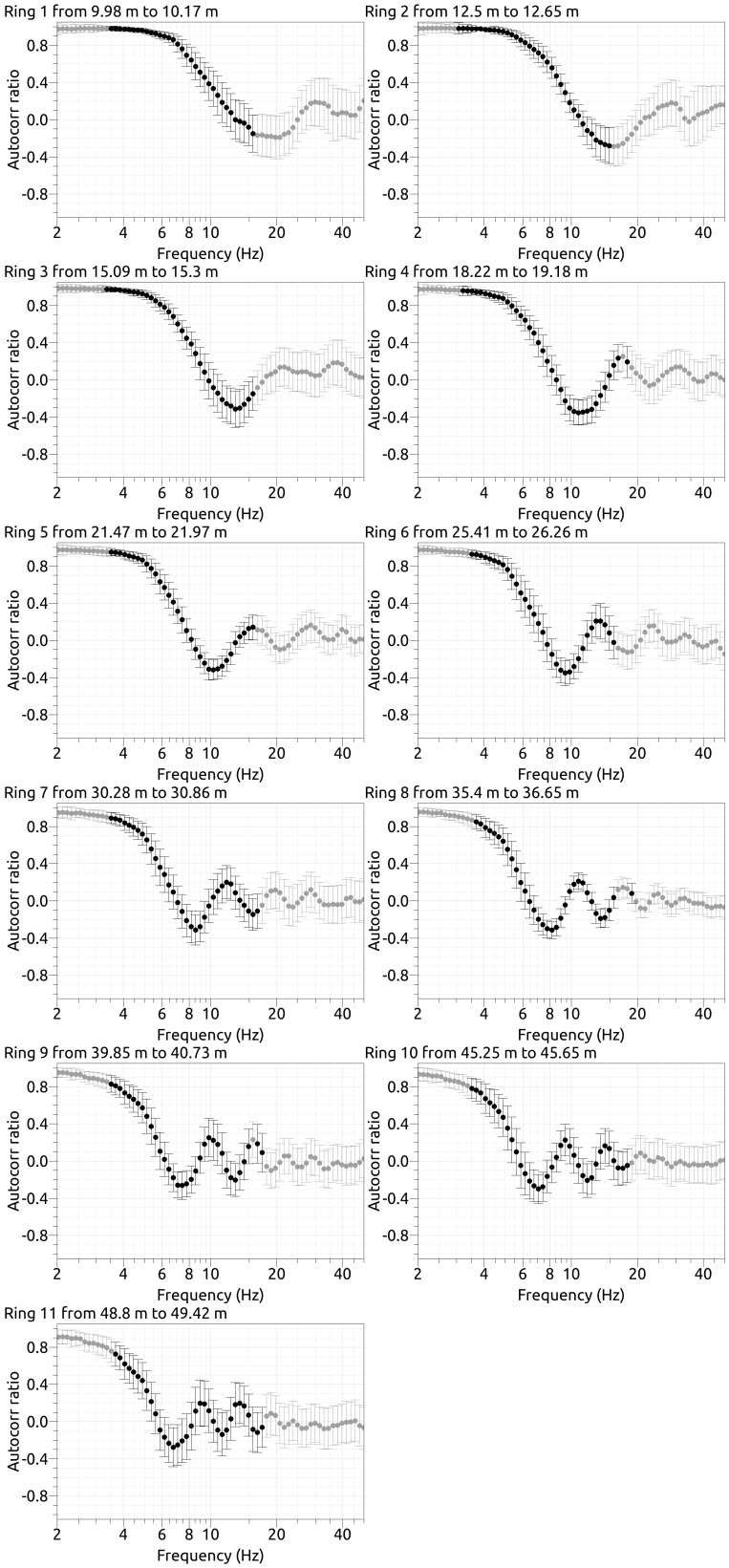

Figure 12: SPAC curves for array 1. The black data points contributed to the dispersion curve estimation.

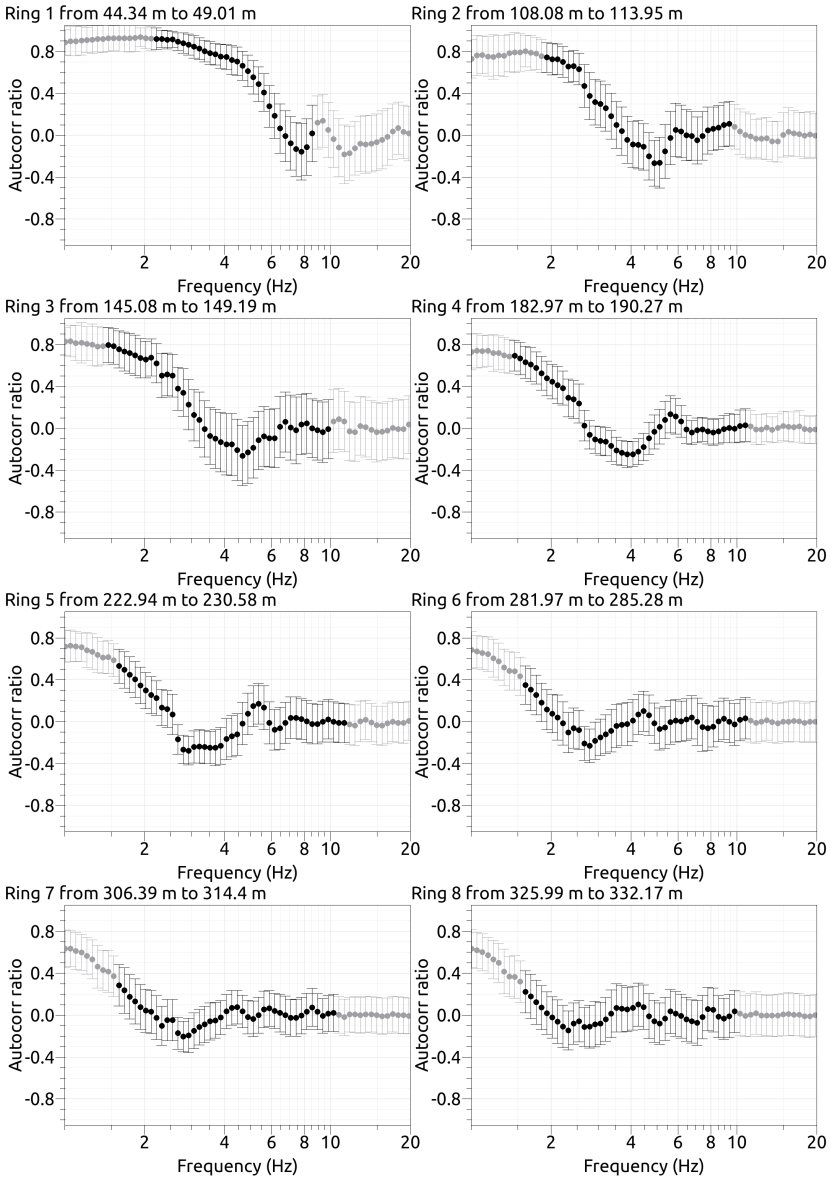

Figure 13: SPAC curves for array 2. The black data points contributed to the dispersion curve estimation.

3.4 Active measurement results

3.4.1 Seismic refraction

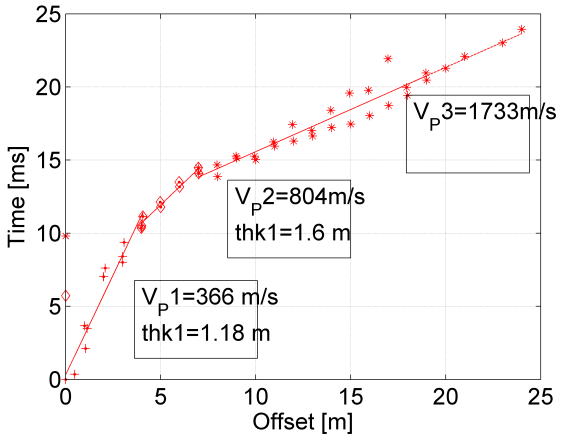

Figure 14: Results of the seismic refraction analysis using the shotpoints HAMMER1, HAMMER2 and HAMMER3. The first arrival times at the different geophones can be explained by three layers at the shallow surface.

The results of the seismic refraction are shown in Fig. 14. The first arrivals at the different geophone locations are well explained by a three-layer model at the shallow surface. The values for the thickness and the P-wave velocities determined by refraction will be used to fix the superficial structure in the inversions.

3.4.2 MASW

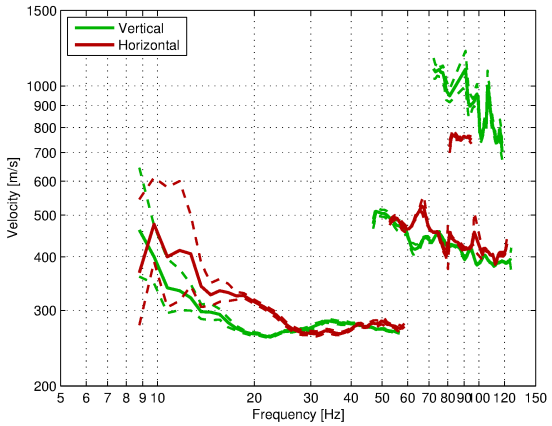

Figure 15: Results of the seismic refraction analysis using the shotpoints HAMMER1, HAMMER2 and HAMMER3. The first arrival times at the different geophones can be explained by three layers at the shallow surface.

The MASW (Park et al., 1999) processing (Fig. 15) retrieves three different modes of Rayleigh waves in different frequency ranges.

3.5 Summary

Fig. 16 gives an overview of the dispersion and ellipticity curves determined by the different methods. The Love wave dispersion curves for array 1 are in good agreement for the 3C-HRFK and the WaveDec methods. For array 2, both have rather different results, but especially WaveDec did not yield good results for this array. It seems reasonable to identify the curve for array 1 as the fundamental Love wave mode, the attribution of the array 2 curve is not clear.
For the Rayleigh waves, we can clearly identify the dispersion curve of the fundamental mode with the data from the first array. The data from both components of 3C-HRFK, WaveDec, SPAC and MASW (at least the vertical component) coincide for the largest part. SPAC retrieves the curve to lower frequencies, the 3C-HRFK result from the radial component differs below 10 Hz and the dispersion curves from SPAC also differ. Data belonging to the fundamental mode at lower frequencies or to the first harmonic mode are measured with the larger array. The agreement between 3C-HRFK, WaveDec and SPAC is still quite good. A part of the first harmonic mode can be seen on the vertical component in the smaller array between 12 and 30 Hz. MASW yields some higher modes above 50 Hz, but their mode number is unclear.
The ellipticity curves for the different methods differ a lot. The WaveDec curve for array 2 is unrealistic, The 3C-HRFK curve from the vertical component in array 1 is mostly in good agreement with the RayDec curve and also with the WaveDec curve for array 1 between 8 and 20 Hz. The 3C-HRFK curves from the large array are not convincing. Finally, the RayDec curve and the WaveDec curve for array 1 are in quite good agreement as both indicate a singular trough between 6 and 7 Hz, but the RayDec curve is not so clear with singular peaks and troughs. The peak on the RayDec curve is seen at 2.5 Hz. The bad performances of the processing in array 2 are probably due to lateral heterogeneities within the array, as can be observed from the H/V curves.

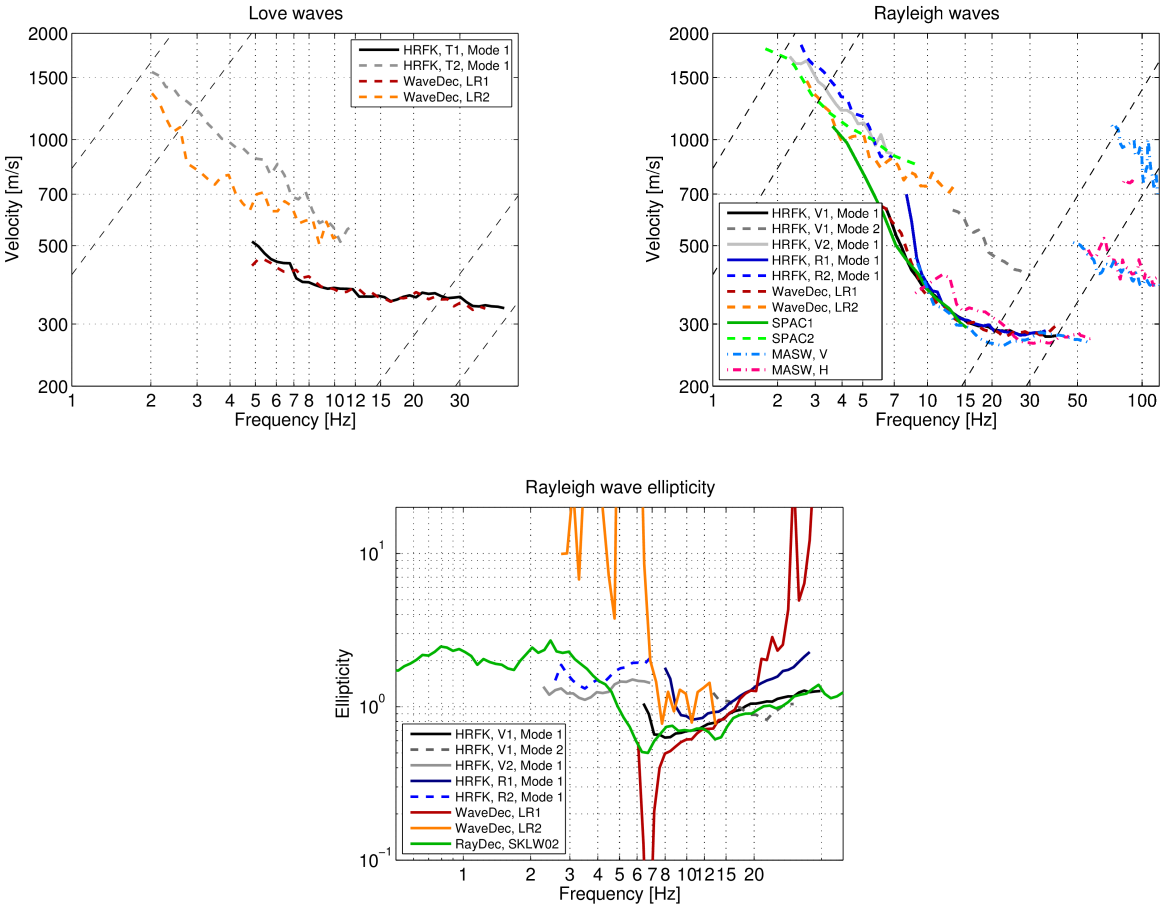

Figure 16: Overview of the Love and Rayleigh wave dispersion curves as well as the ellipticity curves of all measurements. The dashed lines indicate the theoretical resolution limits of the respective arrays (the upper frequency limits corresponds to array 1, the lower one to array 2). The RayDec ellipticity curves correspond to station SKLW02.

4 Data inversion

4.1 Inversion data

For the inversions, the dispersion curve of the fundamental Rayleigh wave mode was combined from the 3C-HRFK analysis (vertical component) of both arrays. The data above 4.2 Hz from the larger array have not been used because they deviate from the SPAC data and are probably biased by the first harmonic mode. The dispersion curve of the second mode measured by 3C-HRFK in the small array was used as the first harmonic mode.
The dispersion curve obtained by 3C-HRFK on the transverse component in the small array was used as dispersion curve for the fundamental Love wave mode. As the mode association of the measurements in the second array were unclear, these data have not been used in the inversion.
The Rayleigh wave ellipticity curve used in the inversion is combined from the RayDec and WaveDec results. WaveDec was used above 6.0 Hz, i.e. for a part including the singularity of the trough and frequencies above. The data around the trough have very high measurement errors, but were included in the inversion successfully. Below 6.0 Hz, the RayDec results were used, but the area just around the fundamental frequency was removed to allow the inversion algorithm to find a singular peak here.

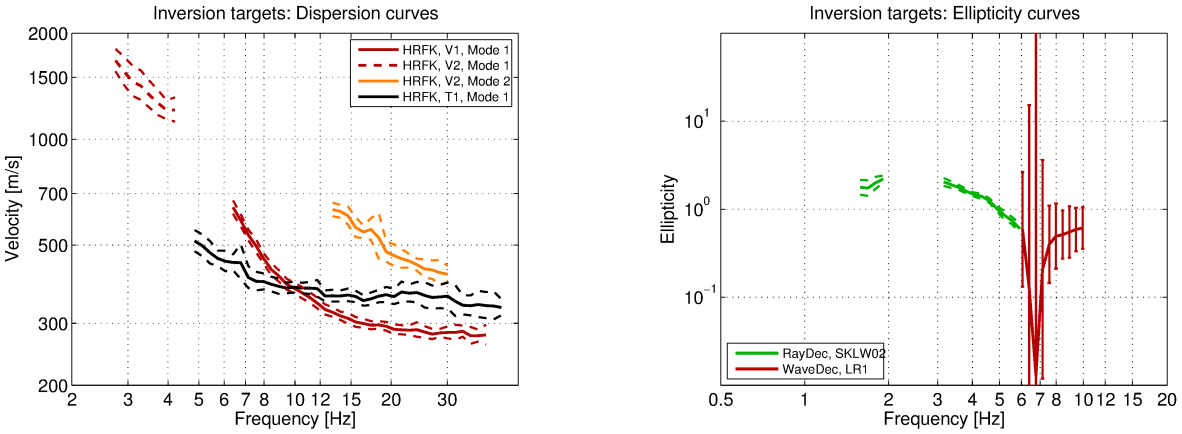

Figure 17: Overview of the dispersion and ellipticity curves used as targets for the different inversions.

Table 4: List of the data curves used as targets in the inversions.

Array	Method	Wave type	Mode	Curve type	Frequency range [Hz]
1	HRFK (V)	Rayleigh	fundamental	dispersion	6.4 - 38.5
2	HRFK (V)	Rayleigh	fundamental	dispersion	2.7 - 4.2
1	HRFK (V)	Rayleigh	harmonic	dispersion	13.3 - 30.0
1	HRFK (T)	Love	fundamental	dispersion	5.2 - 44.0
1	RayDec (SKLW02)	Rayleigh	fundamental	ellipticity	1.6 - 2.0
1	RayDec (SKLW02)	Rayleigh	fundamental	ellipticity	3.2 - 5.8
1	WaveDec LR1	Rayleigh	fundamental	ellipticity	6.0 - 9.8

4.1.1 Inversion parameterization

The resulting structure of the seismic refraction measurement was used as superficial structure. Therefore, we fixed a first layer of 1.18 m thickness with $v_P = 366\,m/s$ and a second layer with 1.6 m thickness and $v_P = 804\,m/s$. The P-wave velocity of the third layer was fixed to $1\,733\,m/s$. The shear-wave velocity of these superficial layers was left variable. Five different inversions with four to eight layers (including bedrock) were performed. Another inversion was done with a fixed depth approach, where layers below the three superficial layers were fixed to 5, 10, 15, 20, 30, 40, ..., 90, 100 m. The density was fixed in the inversions to $2\,000\,kg/m^3$ in the sedimentary layers and to $2\,300\,kg/m^3$ in the bedrock.

4.2 Inversion results

We performed a total of six inversions with different parameterizations (see Table 5). Each inversion run produced 200 000 total models in order to assure a good convergence of the solution. The results of the different inversions are shown in Figs 18 - 23.
Except for the four-layer inversion, all inversions yielded similar minimum misfit values. This indicated that the inversion data are fitted with similar quality, but the best models may well differ. The four-layer model has a significantly larger misfit than the other models. This comes mainly from the bad fit of the fundamental Rayleigh wave mode's dispersion and ellipticity curves.
All the other inversions succeed to fit all data curves in a good way. The inversions with flexible layer depth yield similar results, indicating that the measured data can be fitted well with only five layers, even if gradients in the velocity structures caused by the increasing pressure with depth would be more realistic. All inversions with flexible layer depth find bedrock depths of around 60 m. The fixed-depth inversion shows a different velocity profile, which is mainly increasing linearly and has a major velocity increase between 80 and 100 m depth. However, the data are fitted similarly well and the resulting minimum misfit value is only slightly higher than for the other inversions. All inversions except the four-layer inversion are accepted as reasonable inversions.

Table 5: List of inversions

Inversion	Number of layers	Number of models	Minimum misfit
SKLW04	4	200 000	3.256
SKLW05	5	200 000	1.544
SKLW06	6	200 000	1.470
SKLW07	7	200 000	1.545
SKLW08	8	200 000	1.574
SKLWfix	15	200 000	1.609

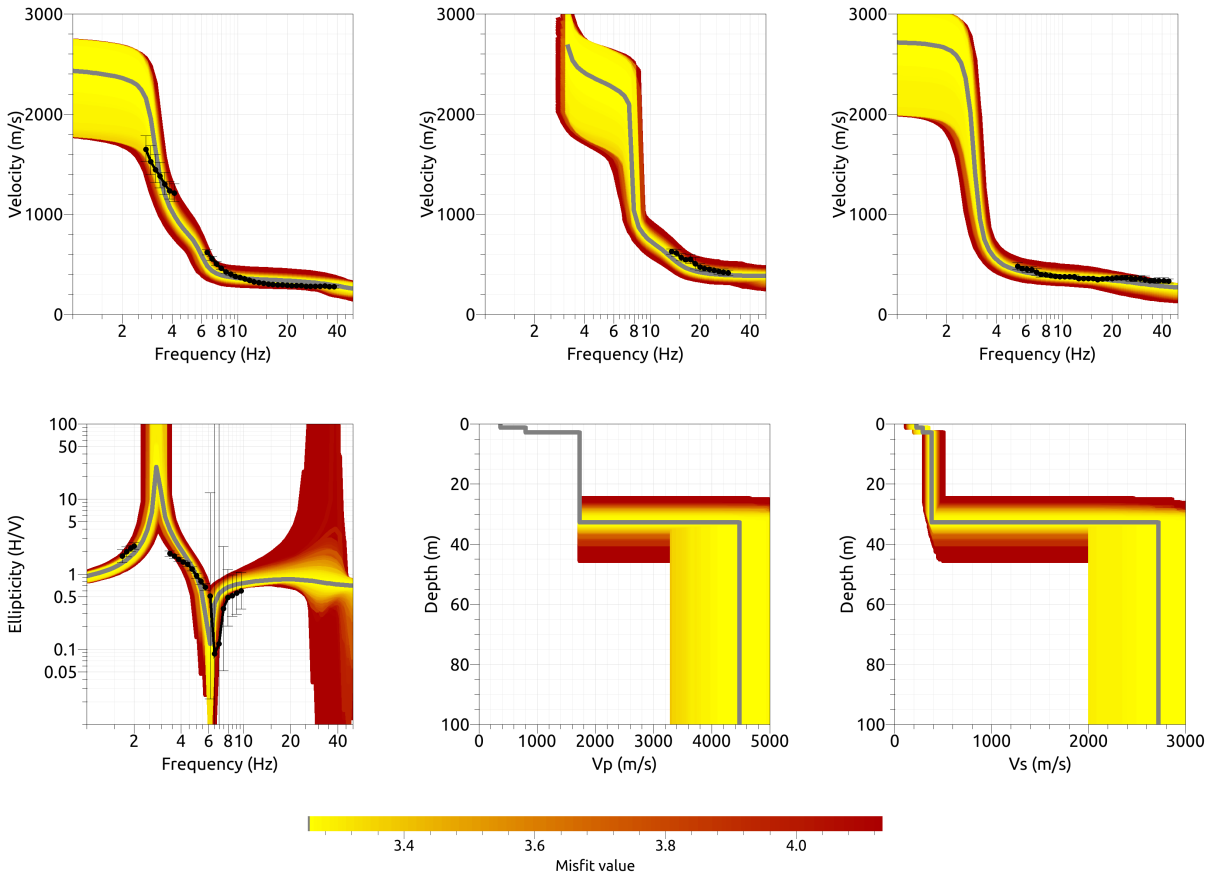

Figure 18: Inversion SKLW04: Rayleigh wave fundamental mode dispersion curve (top left), Rayleigh wave harmonic mode dispersion curve (top center), Love wave fundamental mode dispersion curve (top right), Rayleigh wave fundamental mode ellipticity curve (bottom left), P-wave velocity profiles (bottom center) and S-wave velocity profiles (bottom right). The black dots indicate the data points used for the inversion, the gray line indicates the best-fitting model.

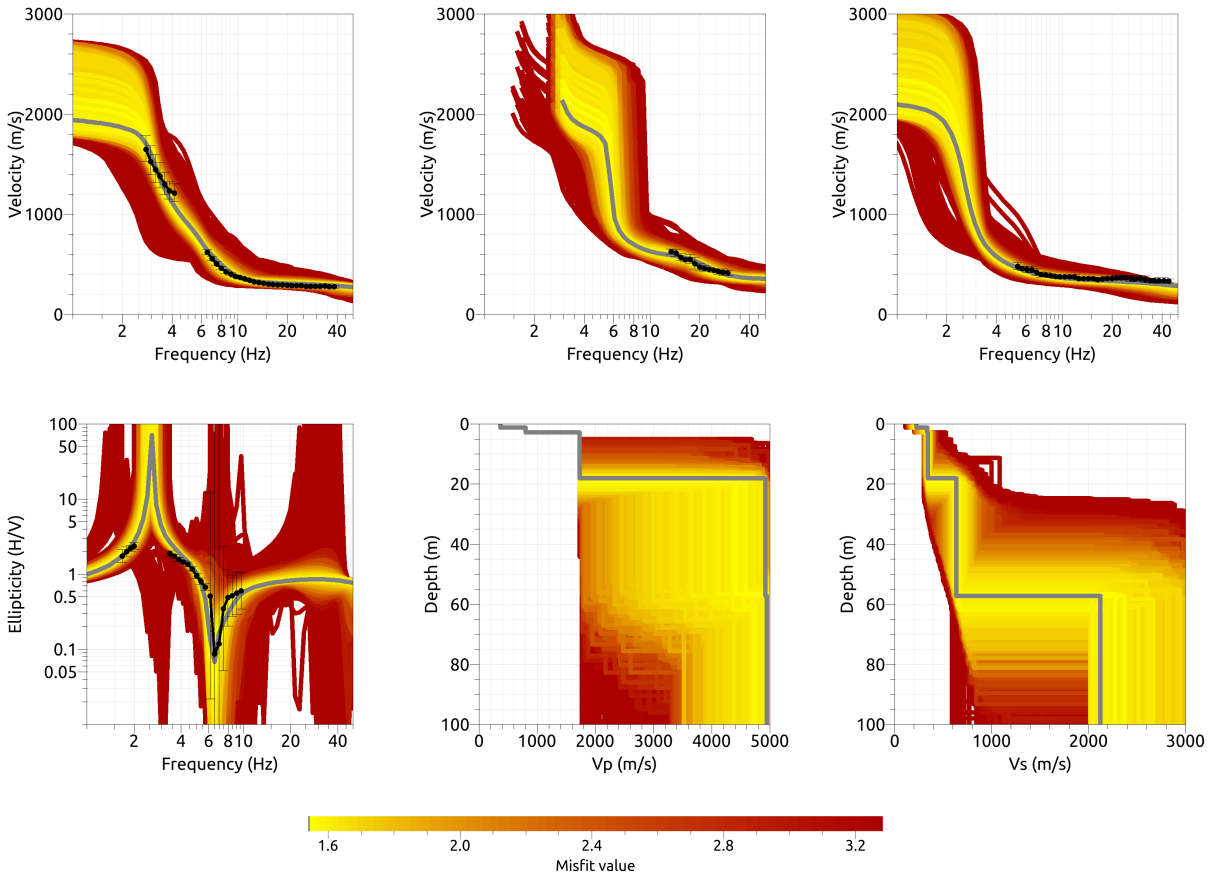

Figure 19: Inversion SKLW05: Rayleigh wave fundamental mode dispersion curve (top left), Rayleigh wave harmonic mode dispersion curve (top center), Love wave fundamental mode dispersion curve (top right), Rayleigh wave fundamental mode ellipticity curve (bottom left), P-wave velocity profiles (bottom center) and S-wave velocity profiles (bottom right). The black dots indicate the data points used for the inversion, the gray line indicates the best-fitting model.

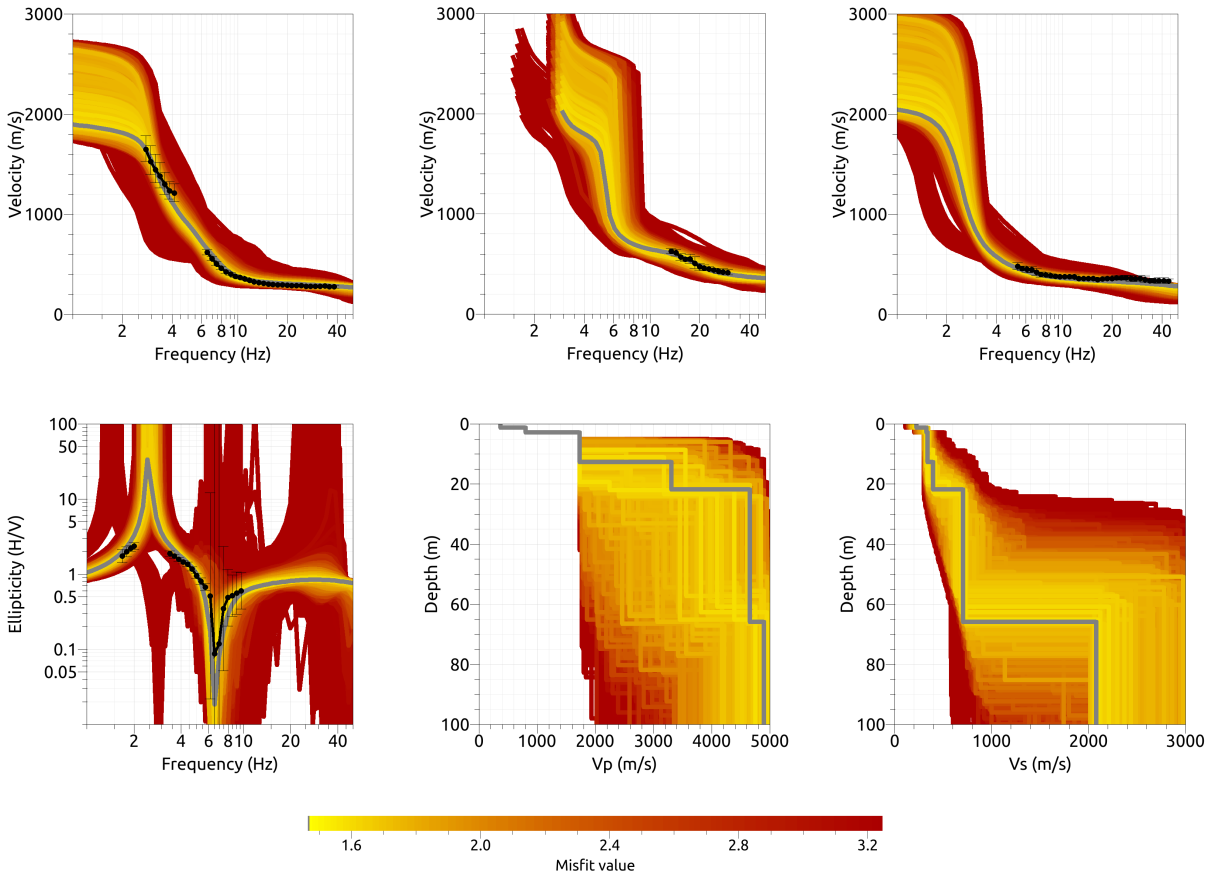

Figure 20: Inversion SKLW06: Rayleigh wave fundamental mode dispersion curve (top left), Rayleigh wave harmonic mode dispersion curve (top center), Love wave fundamental mode dispersion curve (top right), Rayleigh wave fundamental mode ellipticity curve (bottom left), P-wave velocity profiles (bottom center) and S-wave velocity profiles (bottom right). The black dots indicate the data points used for the inversion, the gray line indicates the best-fitting model.

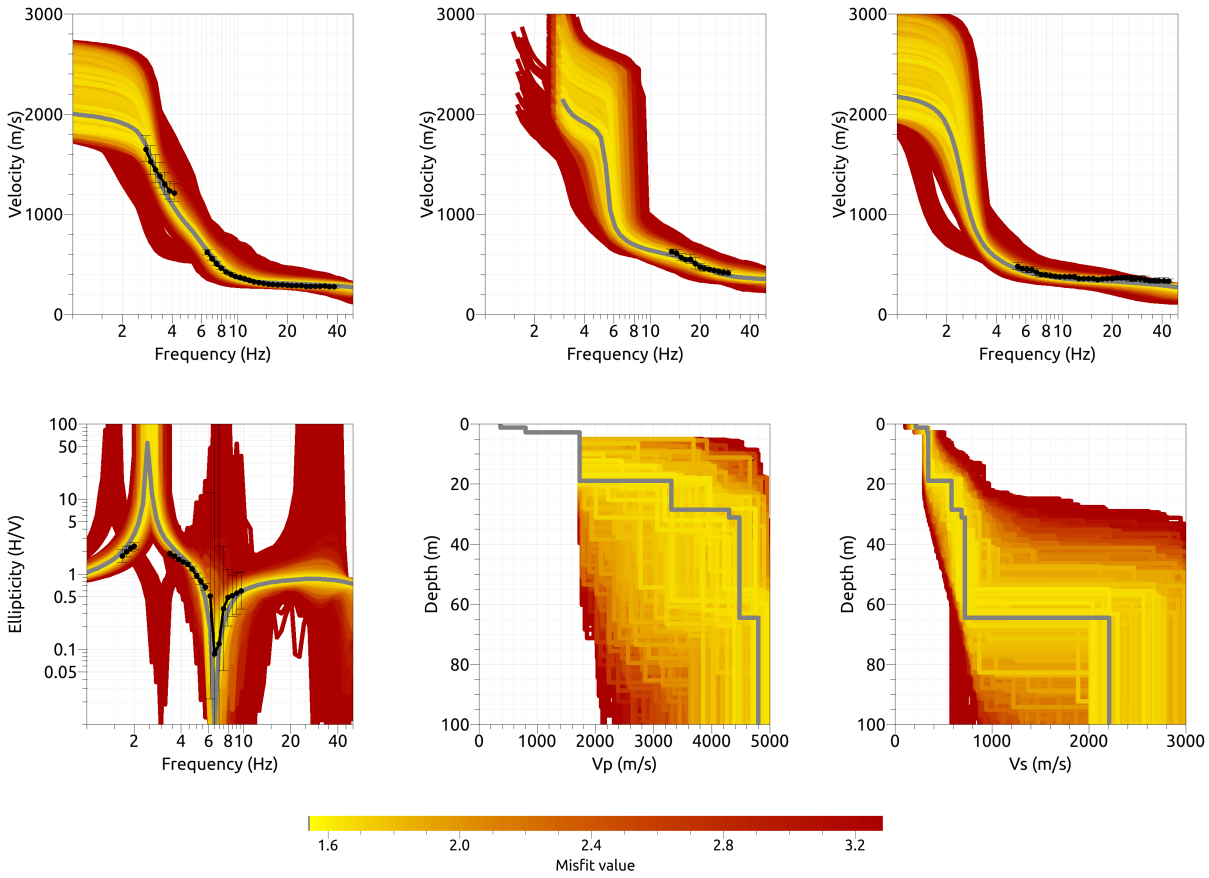

Figure 21: Inversion SKLW07: Rayleigh wave fundamental mode dispersion curve (top left), Rayleigh wave harmonic mode dispersion curve (top center), Love wave fundamental mode dispersion curve (top right), Rayleigh wave fundamental mode ellipticity curve (bottom left), P-wave velocity profiles (bottom center) and S-wave velocity profiles (bottom right). The black dots indicate the data points used for the inversion, the gray line indicates the best-fitting model.

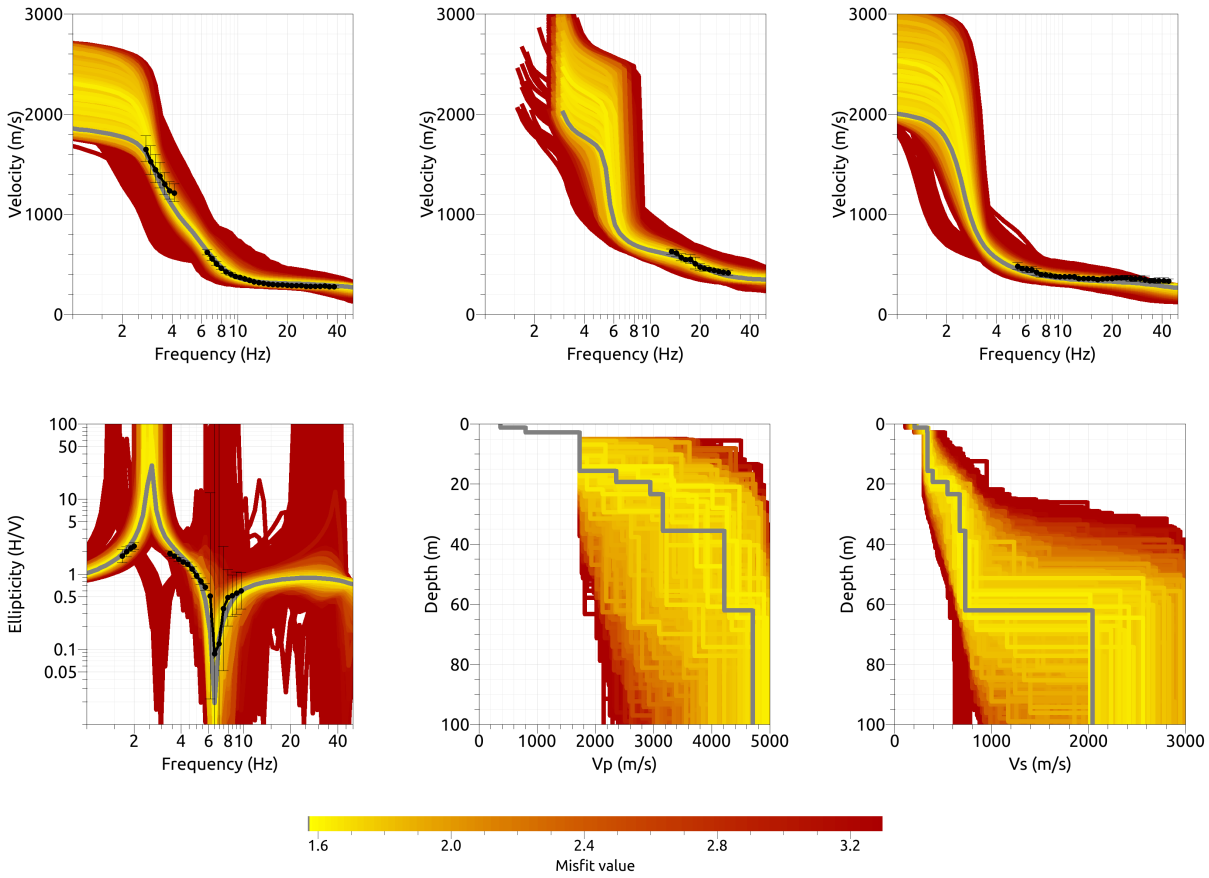

Figure 22: Inversion SKLW08: Rayleigh wave fundamental mode dispersion curve (top left), Rayleigh wave harmonic mode dispersion curve (top center), Love wave fundamental mode dispersion curve (top right), Rayleigh wave fundamental mode ellipticity curve (bottom left), P-wave velocity profiles (bottom center) and S-wave velocity profiles (bottom right). The black dots indicate the data points used for the inversion, the gray line indicates the best-fitting model.

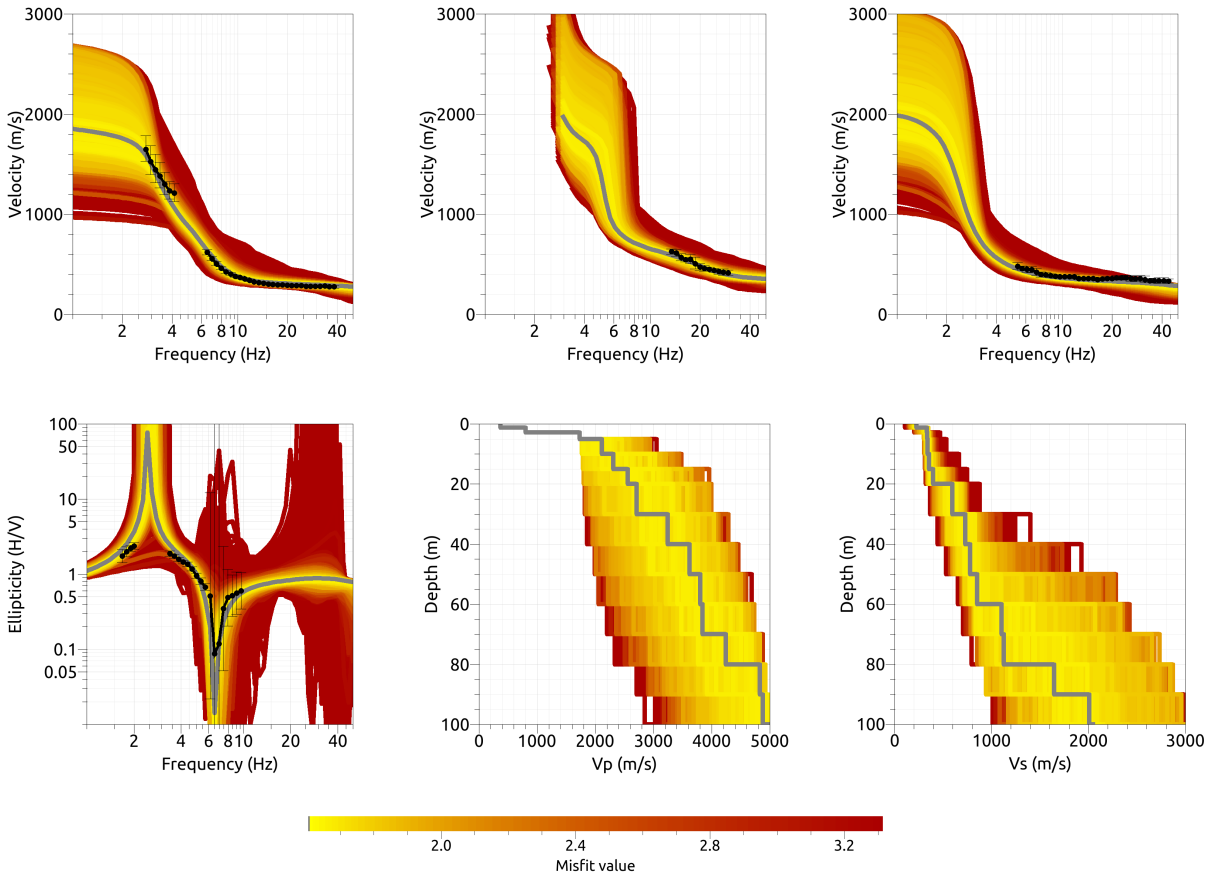

Figure 23: Inversion SKLWfix: Rayleigh wave fundamental mode dispersion curve (top left), Rayleigh wave harmonic mode dispersion curve (top center), Love wave fundamental mode dispersion curve (top right), Rayleigh wave fundamental mode ellipticity curve (bottom left), P-wave velocity profiles (bottom center) and S-wave velocity profiles (bottom right). The black dots indicate the data points used for the inversion, the gray line indicates the best-fitting model.

4.2.1 Discussion of the inversion result

The best-fitting models of all inversions are shown in Fig. 24.
The result of the four-layer inversion clearly differs from the results of the other inversions. The inversions with free layer depths are very similar, especially the ones with six to eight layers. For these inversions, the addition of another layer in the inversion does not significantly change the result. Apart from the fixed depth structure at the superficial 3 m, these inversions yield a first small velocity contrast around 20 m and a second larger velocity contrast around 64 m, which could be interpreted as the bedrock depth.
However, the inversion with the fixed depth approach yielded in a similar fitting of the data curves, but differs in the resulting velocity structure. It shows a rather linear increase which is in perfect agreement with the other inversions in the upper 50 m. The bedrock velocity of around 2 000 m/s is again in perfect agreement with the other inversions, but the intermediate velocity increase is different as there are two main steps at 60 and 80 m depth. The average V_{S30} value of the best-fitting models for the inversions with five to eight layers and the fixed depth approach is $402 \pm 6\, m/s$.

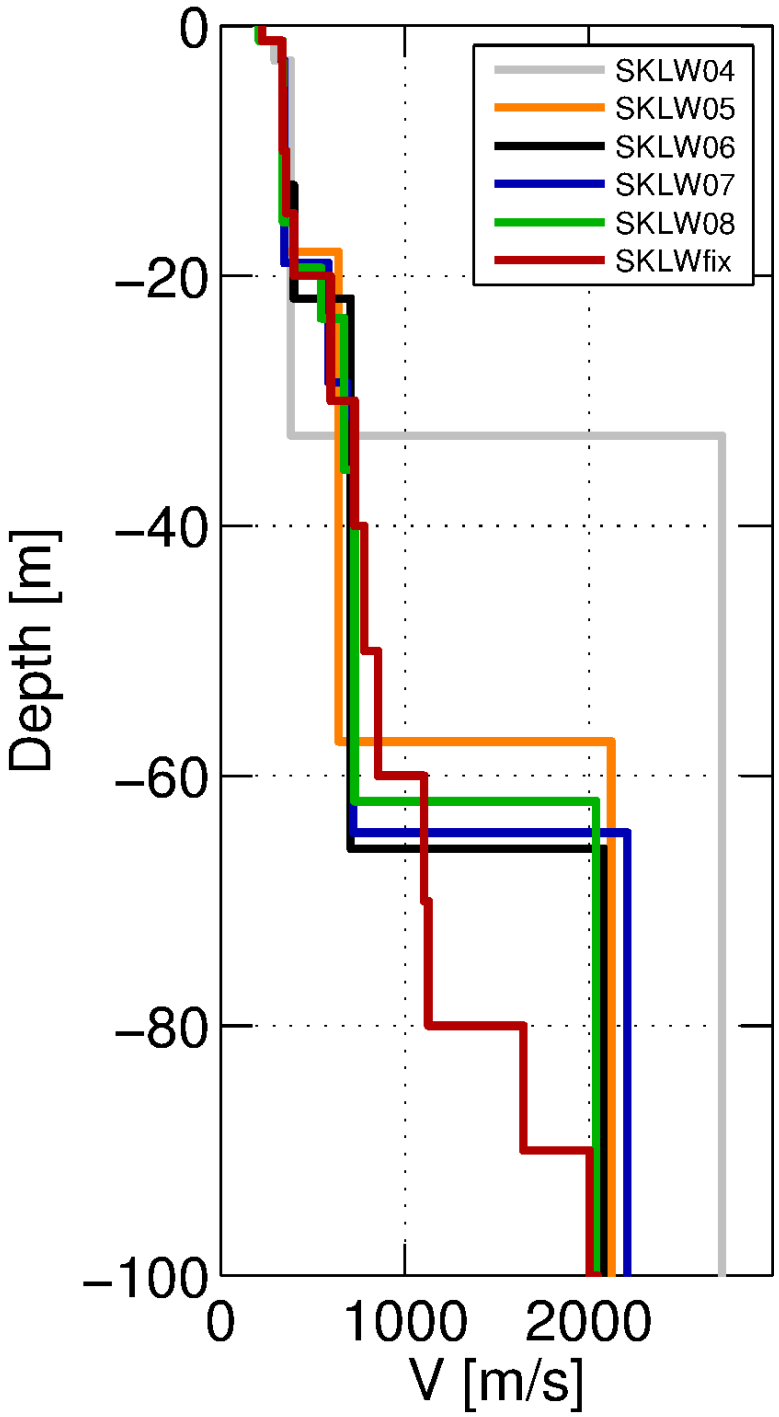

Figure 24: Overview of shear-wave velocity profiles of the best-fitting models of all inversions.

4.3 SH amplification

A comparison between the empirical amplification at station SKLW and the SH transfer function of the best models of the inversions is shown in Fig. 25. Both curves refer to the reference rock profile defined by Poggi et al. (2011). The empirical amplification for station SKLW is based on only one earthquake so far, so that it is not very reliable yet. With values around 10, the empirical amplification is much higher than the theoretical amplification for the underground models. However, the frequencies where the peaks lie in both curves are in quite good agreement.

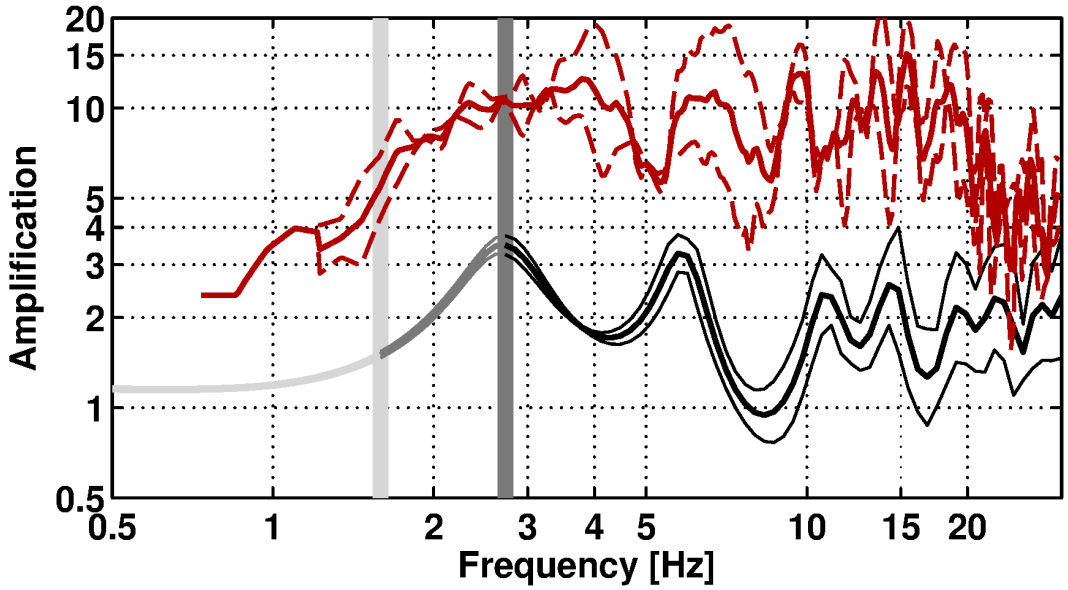

Figure 25: Comparison between the modeled amplification for the best models of the five different inversions with at least five layers (black, with standard deviation) and the empirical amplification measured at station SKLW (red, with standard deviation). The black curves are constrained by the dispersion curves, the light grey curves are not constrained by the data.

4.4 Quarter-wavelength representation

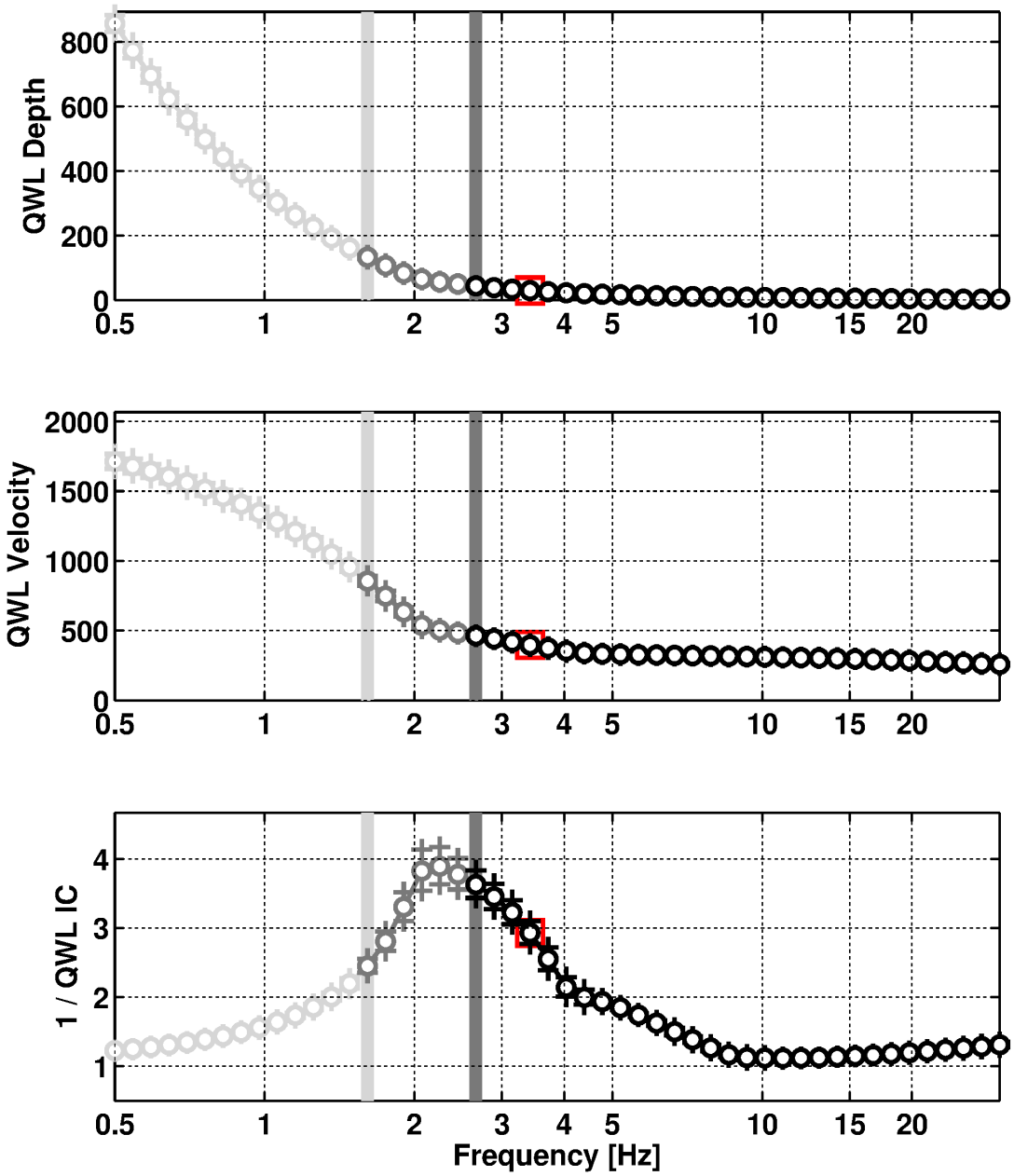

Figure 26: Quarter wavelength representation of the velocity profile for the best models of the five inversions with at least five layers (top: depth, center: velocity, bottom: inverse of the impedance contrast). The black curves are constrained by the dispersion curves, the light grey curves are not constrained by the data. The red square corresponds to V_{S30}.

5 Conclusion

We performed a passive array measurement with two different configurations to characterize the underground under station SKLW, close to the airport of Zurich. In addition, we performed active seismic measurements with geophones and an additional experiment of sledgehammering inside the passive array.
The dispersion curves for both Love and Rayleigh waves could be measured well over a wide frequency range with the smaller array. In the larger array, the quality of the measurements was lower, but it was still possible to retrieve dispersion curves for Love and Rayleigh waves there. The ellipticity measurements of the different techniques differed, but it is possible to define a curve with the RayDec curve at lower frequencies and the WaveDec curve at higher frequencies. The seismic refraction experiment yielded a ground structure for the superficial 3 m, which was subsequently used in the inversions for the deeper structure.
The joint inversion of Love and Rayleigh wave dispersion curve and the ellipticity curve showed that all models with at least five layers can well fit the measurements. The inversions with free layer depth yield a soil structure with a major velocity contrast at around 64 m depth. Another inversion with the fixed depth approach was in good agreement with the other inversions down to 50 m, but differed at deeper layers.
The V_{S30} of the best models is about 402 m/s.

Acknowledgements

The authors thank Marthe Faber and David Farsky for their help during the array measurements.

References

Aki, K. (1957). Space and time spectra of stationary stochastic waves, with special reference to microtremors. *Bull. Earthquake Res. Inst. Tokyo Univ.*, 35:415–456.

Bettig, B., Bard, P.-Y., Scherbaum, F., Riepl, J., Cotton, F., Cornou, C., and Hatzfeld, D. (2001). Analysis of dense array noise measurements using the modified spatial auto-correlation method (SPAC): application to the Grenoble area. *Boll. Geof. Teor. Appl.*, 42:281–304.

Burjánek, J., Gassner-Stamm, G., Poggi, V., Moore, J. R., and Fäh, D. (2010). Ambient vibration analysis of an unstable mountain slope. *Geophys. J. Int.*, 180:820–828.

Burjánek, J., Moore, J. R., Molina, F. X. Y., and Fäh, D. (2012). Instrumental evidence of normal mode rock slope vibration. *Geophys. J. Int.*, 188:559–569.

Fäh, D., Wathelet, M., Kristekova, M., Havenith, H., Endrun, B., Stamm, G., Poggi, V., Burjanek, J., and Cornou, C. (2009). Using ellipticity information for site characterisation. NERIES deliverable JRA4 D4, available at http://www.neries-eu.org.

Hobiger, M., Bard, P.-Y., Cornou, C., and Le Bihan, N. (2009). Single station determination of Rayleigh wave ellipticity by using the random decrement technique (RayDec). *Geophys. Res. Lett.*, 36.

Maranò, S., Fäh, D., and Lu, Y. M. (2014). Sensor placement for the analysis of seismic surface waves: sources of error, design criterion and array design algorithms. *Geophys. J. Int.*, 197:1566–1581.

Maranò, S., Hobiger, M., and Fäh, D. (2016). Analysis of rayleigh waves with circular wavefront: a maximum likelihood approach. *submitted to GJI*.

Maranò, S., Reller, C., Loeliger, H.-A., and Fäh, D. (2012). Seismic waves estimation and wavefield decomposition: Application to ambient vibrations. *Geophys. J. Int.*, 191:175–188.

Park, C. B., Miller, R. D., and Xia, J. (1999). Multichannel analysis of surface waves. *Geophysics*, 64:800–808.

Poggi, V., Edwards, B., and Fäh, D. (2011). Derivation of a reference shear-wave velocity model from empirical site amplification. *Bull. Seismol. Soc. Am.*, 101:258–274.

Poggi, V. and Fäh, D. (2010). Estimating Rayleigh wave particle motion from three-component array analysis of ambient vibrations. *Geophys. J. Int.*, 180:251–267.